Chemical Science

ROYAL SOCIETY OF CHEMISTRY

EDGE ARTICLE

View Article Online
View Journal | View Issue

Cite this: *Chem. Sci.*, 2024, **15**, 8959

All publication charges for this article have been paid for by the Royal Society of Chemistry

A bifunctional primitive strategy induces enhancements of large second harmonic generation and wide UV transmittance in rare-earth borates containing $[B_5O_{10}]$ groups†

Shuaifeng Li,[a] Weiming Li,[a] Xiang Li,[a] Guangsai Yang,[a] Ning Ye,[a] Zhanggui Hu,[a] Yicheng Wu[a] and Conggang Li *[ab]

Received 20th March 2024
Accepted 3rd May 2024

DOI: 10.1039/d4sc01853b

rsc.li/chemical-science

Strong second-harmonic generation (SHG) and a short ultraviolet (UV) cutoff edge are two crucial yet often conflicting parameters that must be finely tuned in the exploration of nonlinear optical (NLO) materials. In this study, two new rare earth borate NLO crystals, $K_7BaSc_2B_{15}O_{30}$ (KBSBO) and $Rb_{21}Sr_{3.8}Sc_{5.2}B_{45}O_{90}$ (RSSBO), were rationally designed through a bifunctional primitive strategy to achieve an optimized balance between favorable SHG efficiency and UV transparency. As anticipated, both KBSBO and RSSBO exhibit a wide UV transparency window below 190 nm. Notably, these tailored crystals display strong SHG responses, with RSSBO achieving a remarkable enhancement in SHG efficiency (2 × KDP), surpassing that of most deep-UV rare earth borates containing $[B_5O_{10}]$ groups known to date. Theoretical calculations and structural analyses reveal that the impressive SHG activities primarily stem from the $[B_5O_{10}]$ groups and $[ScO_6]$ polyhedra. These findings suggest promising potential for KBSBO and RSSBO crystals as beryllium-free deep UV NLO materials.

Introduction

Deep ultraviolet (UV) nonlinear optical (NLO) materials possess the capacity to generate coherent ultraviolet light through laser frequency conversion, and are in great demand for various critical applications, such as information communication, laser medical treatment, and photolithography.[1–9] In recent decades, sustained endeavors have been directed towards the design and fabrication of new deep UV optical crystals to elucidate the SHG process. Thus far, only $KBe_2BO_3F_2$ (KBBF) has demonstrated practical potential for directly generating coherent light below 200 nm.[10] However, the incorporation of highly toxic beryllium in its synthesis raises significant concerns. Moreover, the KBBF crystal displays unfavorable tendencies of layered growth due to its weak interlayer interactions.[11] Hence, there is an imperative need to develop novel deep UV NLO materials that exhibit favorable crystal growth attributes and are devoid of hazardous beryllium.

To pursue deep UV NLO crystals, beyond satisfying the precondition of non-centrosymmetric structure, a wide transparency window and a large SHG response are also indispensable. However, it remains a formidable challenge to simultaneously achieve an intense SHG effect (>1 × KDP) and a short UV cutoff edge (<200 nm), as they present an inverse correlation owing to the inverse proportionality of the SHG coefficients to the function associated with the band-gap.[12–15] The inherent contradiction posed by the stringent performance criteria renders the exploration of deep-UV NLO materials a formidable challenge. In view of this, borates have garnered significant interest which is attributed to their versatile structural geometry and exceptional properties, presenting a promising avenue for advancement in this field. Boron atoms bound to oxygen atoms can form $[BO_2]$, $[BO_3]$, and $[BO_4]$ motifs through sp, sp^2, and sp^3 hybrid orbitals, respectively, leading to the creation of diverse fundamental building blocks (FBBs), such as $[B_2O_5]$, $[B_3O_6]$, $[B_4O_9]$ and $[B_5O_{10}]$, among others, *via* various connection patterns.[16–20] The regulation of the B/O ratio presents a promising strategy for the design of deep UV NLO crystals with high performance. Notably, a variety of deep UV NLO crystals incorporating different FBBs, including β-$Rb_2Al_2B_2O_7$ and $CaZn_2(BO_3)_2$ with $[BO_3]$,[10,21] $Ba_4Ca(B_2O_5)_2F_2$ with $[B_2O_5]$,[22] $Cs_3Zn_6B_9O_{21}$ and $Ca_2B_3O_6X$ (X = Cl, Br) with $[B_3O_6]$,[23,24] $Li_2B_4O_7$ with $[B_4O_9]$,[25] and $K_3B_5O_8(OH)_2$ with $[B_5O_8(OH)_2]$,[26] have been synthesized.

[a]*Tianjin Key Laboratory of Functional Crystal Materials, Institute of Functional Crystal, Tianjin University of Technology, Tianjin 300384, China*

[b]*State Key Laboratory of Crystal Materials, Shandong University, Jinan, 250100, China*

† Electronic supplementary information (ESI) available: Experimental section, additional crystallographic data, the dipole moments for KBSBO and RSSBO, the investigation of B–O bond lengths, PXRD curves, and the partial enlargement of B_5O_{10} units for KBSBO and RSSBO. CCDC 2335307 and 2335374. For ESI and crystallographic data in CIF or other electronic format see DOI: https://doi.org/10.1039/d4sc01853b

In addition to the B–O anionic framework, incorporation of rare earth (RE) cations into borates not only enriches the structural features, but also shows the potential to enhance the SHG activities through the formation of RE-based deformed polyhedra. Importantly, rare earth ions (RE = Sc^{3+}, Y^{3+}, La^{3+}, Lu^{3+}, and Gd^{3+}) are devoid of d–d or f–f electronic transitions, promoting good transparency in the UV spectral region with deep-UV absorption edges below 200 nm. For example, compounds like $RECa_4O(BO_3)_3$ (RE = Y, Gd),[27] $La_2CaB_{10}O_{19}$,[28] and $K_7MY_2B_{15}O_{30}$ (M = Ca, Sr, Ba)[29] exhibit short UV cutoff edges and favorable SHG intensities. The combination of rare earth ions and borates offers a versatile tunability of optical properties.

Building upon the above analysis, we have focused on the rare-earth metal–borate system, resulting in the fabrication of two novel rare-earth borate NLO crystals, $K_7BaSc_2B_{15}O_{30}$ (KBSBO) and $Rb_{21}Sr_{3.8}Sc_{5.2}B_{45}O_{90}$ (RSSBO). These crystals possess an isomorphic structure and crystallize in the acentric *R*32 space group. Interestingly, KBSBO and RSSBO feature remarkably short deep UV absorption cutoff edges below 190 nm, and exhibit enhanced SHG responses (>1 × KDP). Notably, RSSBO shows a remarkable improvement in SHG efficiency (2 × KDP), exceeding that of most deep UV rare earth borates containing $[B_5O_{10}]$ groups. Our findings indicate that the tailored crystals are promising deep UV NLO materials. We present the synthesis, property characterization, and structure–property relationship of KBSBO and RSSBO. This work enriches the structural chemistry of rare earth borates and provides a viable avenue for exploring novel deep UV NLO materials with high performance.

Results and discussion

PXRD and thermal characterizations

The polycrystalline samples of KBSBO and RSSBO were synthesized *via* a solid-phase synthesis process. Fig. 1a and b show the PXRD profiles of the synthesized compounds, which manifest similar diffraction peaks well indexed to standard data, with no additional phase discernible. To probe the thermal stabilities of KBSBO and RSSBO, thermogravimetric (TG) analysis and differential scanning calorimetry (DSC) were conducted. As depicted in Fig. 1c and d, prominent endothermic peaks appear at around 864 and 822 °C for KBSBO and RSSBO, respectively, while no discernible weight loss is

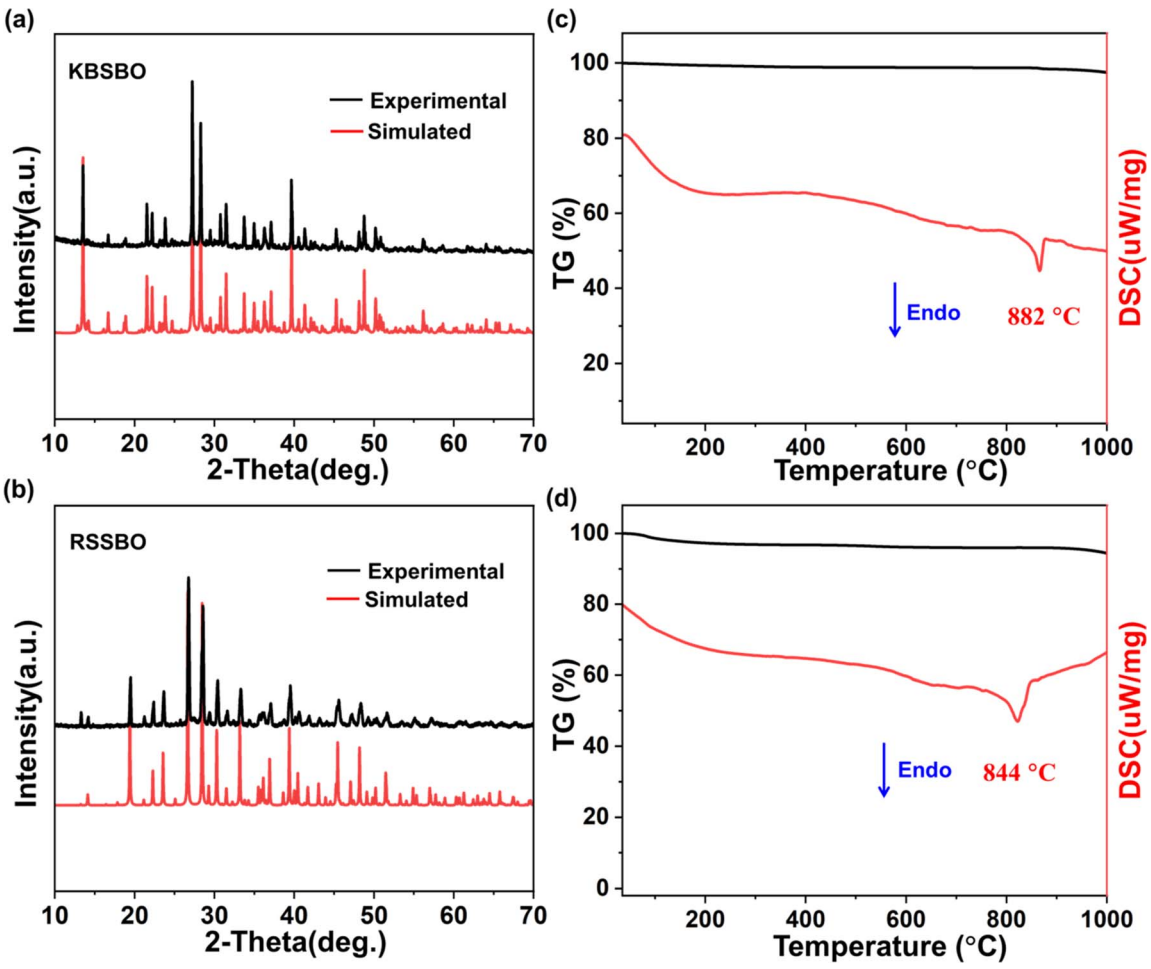

Fig. 1 (a and b) Simulated and experimental PXRD curves for KBSBO and RSSBO, respectively. (c and d) TG–DSC curves for KBSBO and RSSBO, respectively.

observed in the corresponding TG curves over the temperature range, indicating excellent thermal stability of the compounds. Moreover, Fig. S1† demonstrates that the PXRD patterns of KBSBO and RSSBO subjected to annealing above 900 °C are inconsistent with their initial patterns, suggesting that the compounds display an incongruent melting nature.

Structural analyses

The small, transparent crystals of KBSBO and RSSBO were extracted using a flux method. Single-crystal XRD measurements have revealed that both compounds exhibit isostructural features and crystallize in the acentric space group *R*32. Extended crystallographic data and refined structural data including atomic coordinates and equivalent isotropic displacement parameters, bond length and angle information for KBSBO and RSSBO are presented in Tables S1–S5.† In detail, the asymmetric unit of KBSBO contains eight unique potassium sites, two unique barium sites, four unique scandium sites, eleven boron sites, and twenty unique oxygen sites. RSSBO comprises three unique rubidium sites, two unique strontium/scandium sites, three boron sites, and seven unique oxygen sites. As shown in Fig. 2a, the B atoms exhibit two distinct coordination geometries, consisting of $[BO_4]$ tetrahedra and $[BO_3]$ coplanar triangles, which are interconnected to form isolated $[B_5O_{10}]$ clusters. The majority of B–O bond lengths in the two compounds fall within typical values, as observed through an examination of B–O bond lengths in BO_3 units among inorganic metal borates (Table S8†). However, in RSSBO, a distinct $[BO_3]$ unit is present with the B–O bond distances ranging from 1.26 (3) to 1.53 (3) Å, featuring a clamping angle of 17.8° in the O7–B2–O4 configuration (Fig. S2†). This distinct $[BO_3]$ unit can be attributed largely to the fractional occupancy of the O4 and O7 sites owing to the disorder of oxygen atoms, which may be interpreted as dynamically or statically disordered moieties.[30,31] From a structural and performance perspective, this distinct $[BO_3]$ unit has the capability to strengthen the covalent bond, consequently positively impacting optical properties, notably the second-order microscopic polarizability. As illustrated in Fig. 2b, the isolated $[B_5O_{10}]$ groups with distinct orientations extend infinitely along the ac plane in KBSBO and RSSBO, resulting in a pseudo-two-dimensional (2D) layer. In KBSBO, the $[ScO_6]$ and $[BaO_6]$ octahedra are bridged to form three types of $[Sc_2BaO_{12}]$ clusters (Fig. 2c), which are further linked with the pseudo-2D layer to construct a three-dimensional (3D) structural framework (Fig. 2d). On the other hand, in RSSBO, three $[Sc/SrO_6]$ octahedra are interlinked to form a distinct $[Sc_mSr_nO_{12}]$ $(m + n = 3)$ group, which is attributed to the shared joint occupancy by the Sr^{2+} and Sc^{3+} cations at the Wyckoff sites (Fig. 2e). It is facile to envisage that the disparity in the cation radii between Sr^{2+} and Sc^{3+} can induce a greater degree of distortion for the $[Sc/SrO_6]$ octahedra. These $[Sc_mSr_nO_{12}]$ groups and the pseudo-2D layer are further connected to build a 3D network of RSSBO (Fig. 2f). To verify the rationality of the structure, the valence bands of the compounds were calculated, as provided in Tables S2 and S3,† which is consistent with the findings of our structural analysis.

Spectroscopy properties

To assess the optical characteristics, UV–Vis–NIR diffuse reflectance spectra measurements were performed on the polycrystalline forms of KBSBO and RSSBO. As depicted in Fig. 3a and b, both compounds exhibit notably short deep UV absorption cutoff edges below 190 nm. The comparison of transmission ranges between these compounds and other developed RE borates containing $[B_5O_{10}]$ units is summarized in

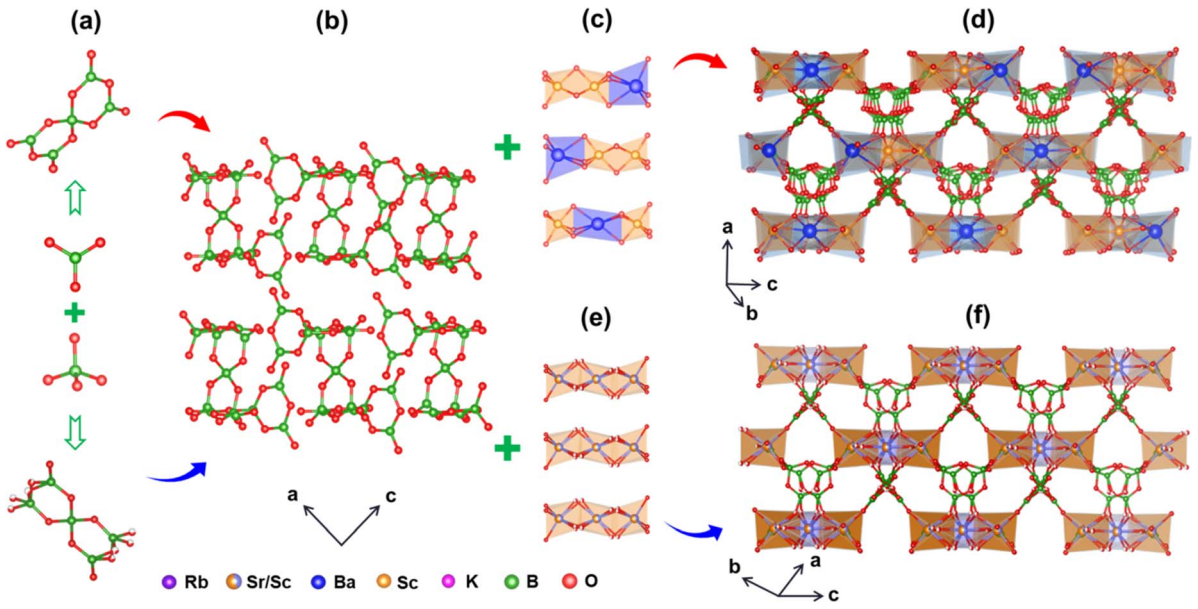

Fig. 2 Structural features of KBSBO and RSSBO. (a) $[BO_3]$, $[BO_4]$ units and $[B_5O_{10}]$ groups. (b) The pseudo-2D layer viewed from the ac plane. (c and d) Presentation of three types of $[Sc_2BaO_{12}]$ groups and the 3D structural framework of KBSBO, respectively. (e and f) Presentation of the $[Sc_mSr_nO_{12}]$ $(m + n = 3)$ group and 3D structural framework of RSSBO, respectively.

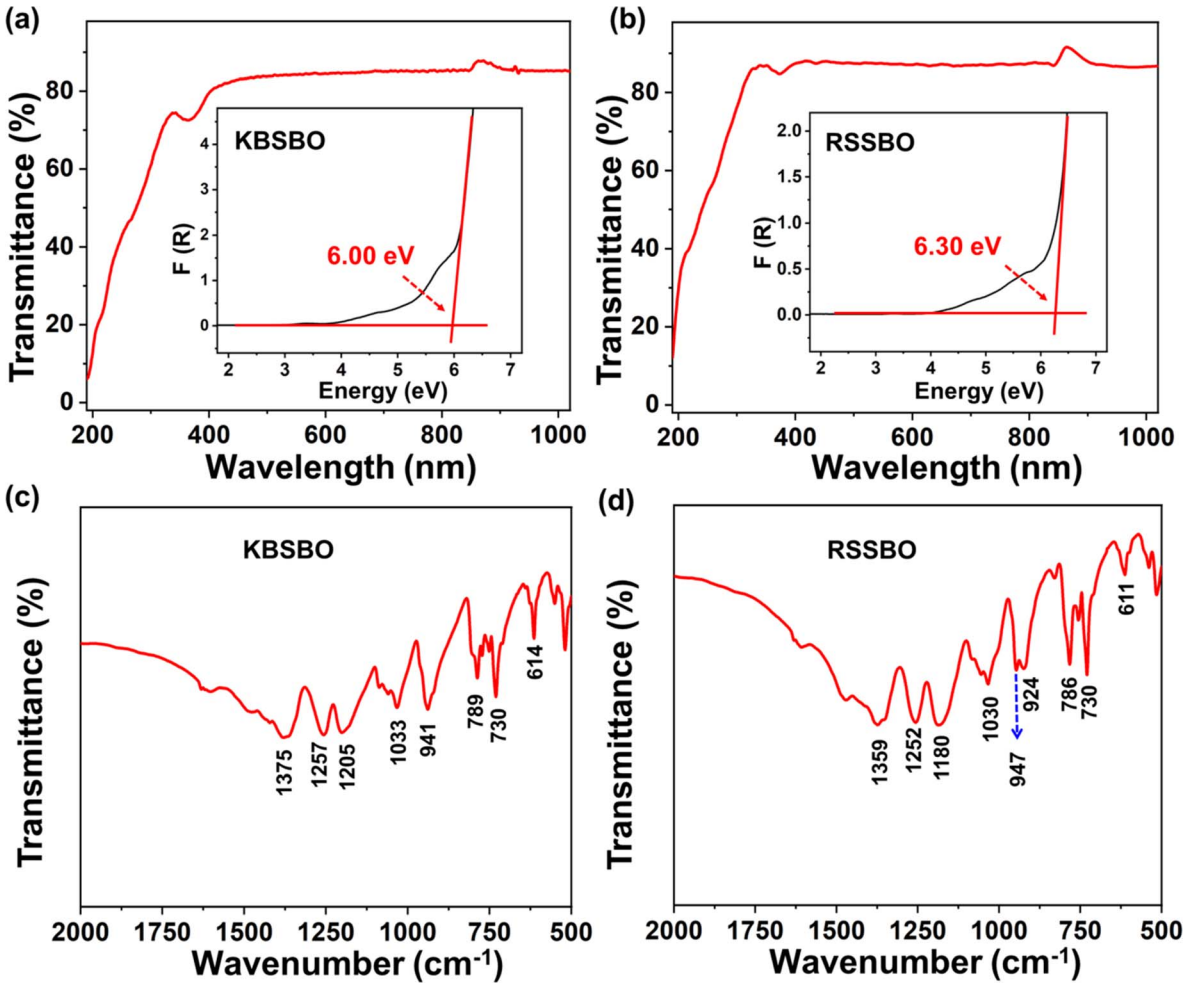

Fig. 3 (a and b) UV–Vis–NIR diffuse reflectance spectra with the corresponding band gaps. (c and d) Infrared spectrum for KBSBO and RSSBO, respectively.

Table 1.[32–42] The favorable optical transmissibility yields large band gaps of approximately 6.00 eV and 6.30 eV for KBSBO and RSSBO, respectively, as determined by the Kubelka–Munk formula (inset of Fig. 3a and b),[43] which is consistent with the results of Tauc plots (Fig. S3†).[44] Furthermore, the infrared (IR) absorption spectra reveal that KBSBO and RSSBO possess similar characteristic peaks in the range of 1000–4000 cm^{-1} (Fig. 3c and d). The peaks located in the range of 1100–1400 cm^{-1} are predominantly assigned to the asymmetric stretching vibrations of the [BO_3] plane triangle, while those observed between 1000 and 1100 cm^{-1} correspond to the symmetric stretching vibrations of [BO_4] groups. The bands falling within the region of 860–1000 cm^{-1} belong to the symmetric stretching vibrations of [BO_3] groups. The bands located between 700 and 860 cm^{-1} are primarily attributed to the symmetric stretching vibration of [BO_4] units. Additionally, the bending vibrations of the [BO_3] and [BO_4] motifs give rise to the peaks between 600 and 700 cm^{-1}. These findings firmly establish the coexistence of the [BO_3] and [BO_4] units in KBSBO and RSSBO, consistent with the previously reported results, and further validate the soundness of the structural analyses.[32–34]

Table 1 UV cutoff edges (in nm) and SHG efficiency (×KDP) for the inorganic metal borates containing an isolated FBB [B_5O_{10}] group in non-centrosymmetric compounds

Compounds	Space group	UV cutoff edges (nm)	SHG (×KDP)
$KB_5O_8 \cdot 4H_2O$ (ref. 26)	*Aba*2	168	0.2
$K_7CdY_2B_{15}O_{30}$ (ref. 32)	*R*32	200	1.6
$K_7CdLu_2B_{15}O_{30}$ (ref. 32)	*R*32	192	1.9
$K_7SrY_2B_{15}O_{30}$ (ref. 33)	*R*32	190	1.1
$Rb_7SrGd_2B_{15}O_{30}$ (ref. 34)	*R*32	190	0.5
$K_3YB_6O_{12}$ (ref. 35)	*R*32	195	0.1
$Rb_3YB_6O_{12}$ (ref. 36)	*R*32	200	0.8
$Rb_3NdB_6O_{12}$ (ref. 37)	*R*32	197	4 × α-SiO_2
$K_6LiCaSc_2B_{15}O_{30}$ (ref. 38)	*R*32	200	0.4
$K_6Li_3Sc_2B_{15}O_{30}$ (ref. 39)	*R*32	190	1.0
$Rb_7CaY_2B_{15}O_{30}$ (ref. 40)	*R*32	195	1.4
$Rb_7SrY_2B_{15}O_{30}$ (ref. 41)	*R*32	190	0.9
$Rb_7SrSc_2B_{15}O_{30}$ (ref. 42)	*R*32	200	0.76
$Rb_7CaSc_2B_{15}O_{30}$ (ref. 42)	*R*32	200	0.8
$K_7BaSc_2B_{15}O_{30}$ (TW)	*R*32	190	1.4
$Rb_7SrSc_2B_{15}O_{30}$ (TW)	*R*32	190	2.0

Second-harmonic generation (SHG) activities

To assess the SHG activities, powder SHG measurements was employed on polycrystalline KBSBO and RSSBO using a modified Kurtz–Perry method under a 1064 nm laser.[45] As depicted in Fig. 4a and b, the SHG intensities of KBSBO and RSSBO consistently increase with particle size and eventually reach a saturation value, suggesting their phase-matchable nature. These compounds exhibit strong SHG efficiency (>1 × KDP) in the particle size range of 180–212 μm, respectively. As intuitively shown in Fig. 4c, RSSBO exhibits a notable improvement in SHG efficiency (2 × KDP), surpassing that of most deep UV rare earth borates containing $[B_5O_{10}]$ groups reported so far.[26,29,32–42] These observed attributes indicate the potential of KBSBO and RSSBO as beryllium-free deep UV nonlinear optical (NLO) crystals.

Structure–property relationship

To deepen the comprehension of the structure–property correlation in the KBSBO and RSSBO compounds, first-principles calculations were conducted to scrutinize their microscopic mechanism. As shown in Fig. 5a and b, both KBSBO and RSSBO display the attributes of direct band gap semiconductors, with the valence band maximum and the conduction band minimum lying within the same Brillouin zone. The band gaps of the two compounds were determined to be 4.05 eV and 4.48 eV, respectively, slightly lower than the experimental values. Furthermore, the density of states (DOS) and the partial density of states (PDOS) reveal the electron orbital distribution near the forbidden band gap of the two compounds, facilitating the analysis of the microscopic mechanism. As depicted in Fig. 5c and d, the valence bands spanning from −15 to −20 eV are predominantly constituted by the B 2s 2p and O 2p orbitals, while those between 15 and 20 eV originate from the B 2p and Sc 3p orbitals. The bands falling in the range of −7 to 7 eV near the valence band top and conduction band bottom are primarily contributed by the B 2p and Sc 3d orbitals, with a slight contribution from Ba 5d or Sr 4d, exhibiting hybridization with the O 2p orbital. It is widely acknowledged that the intrinsic optical properties of materials are closely linked to the electronic transitions in proximity to the forbidden level.

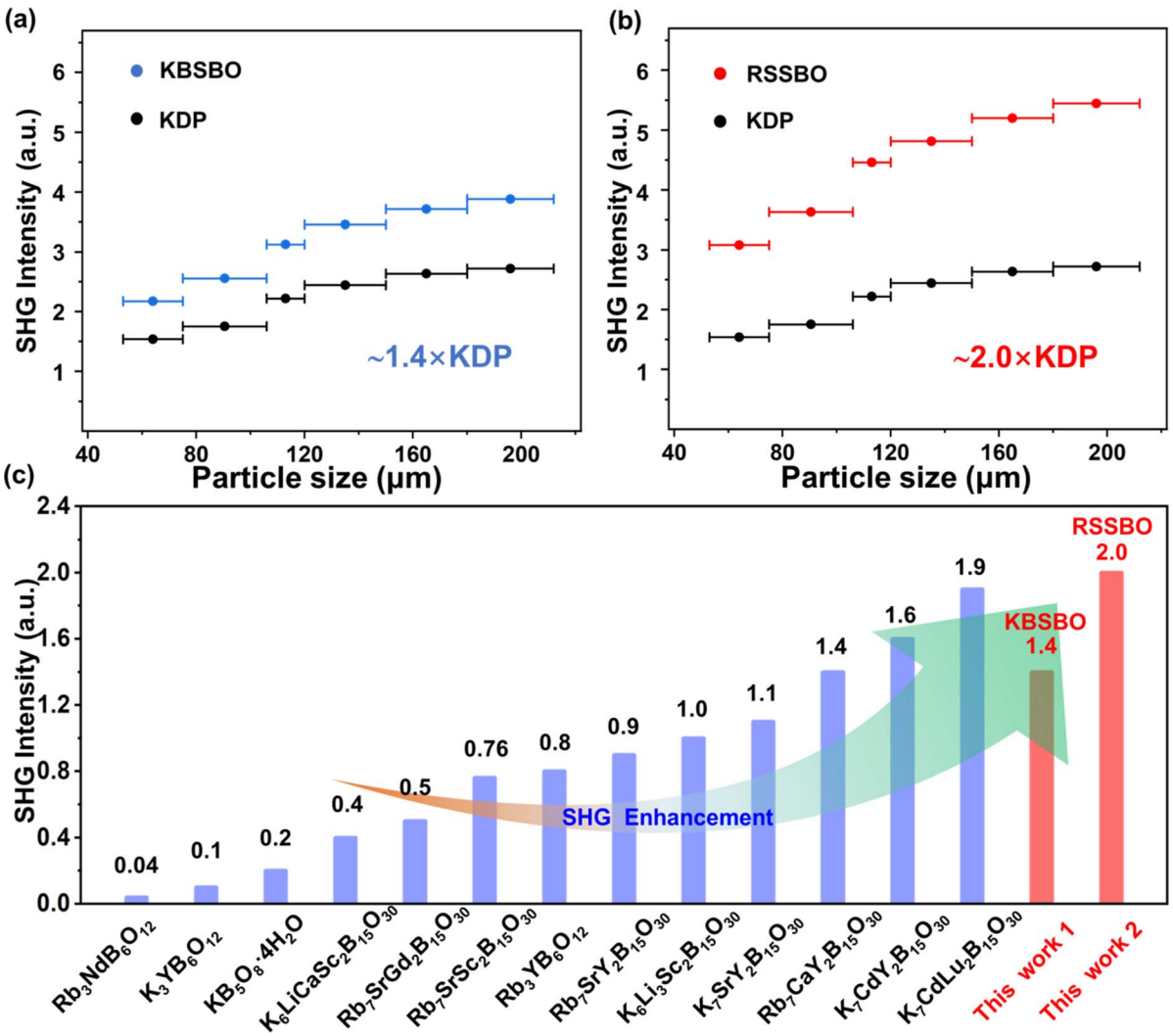

Fig. 4 (a and b) SHG intensity curves with different particle sizes for KBSBO and RSSBO, respectively. (c) The comparison of the SHG activities among KBSBO, RSSBO and other deep UV rare-earth borates containing $[B_5O_{10}]$ groups.

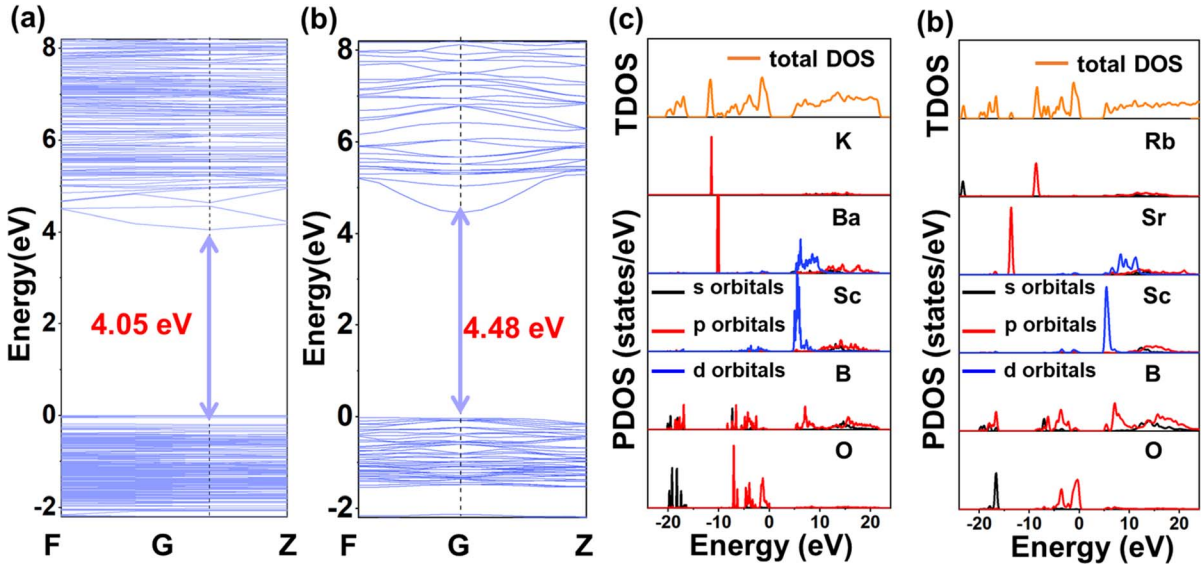

Fig. 5 (a and b) Calculated band structures and (c and d) total and partial density of states for KBSBO and RSSBO, respectively.

Consequently, we deduce that the SHG effect predominantly arises from the $[B_5O_{10}]$ groups and the $[ScO_6]$ octahedra of KBSBO and RSSBO.

To unravel the NLO properties of both compounds, the dipole moments surrounding the $[BO_3]$ planar triangles and $[BO_4]$ tetrahedra, as well as $[ScO_6]$ and $[Sc/SrO_6]$ octahedra were analyzed. This analysis revealed that the primary source of SHG intensity resides in the π-conjugated $[BO_3]$ planar triangles and distortive $[MO_6]$ octahedra (M = Ba, Sr and Sc). Notably, the $[B_{(2)}O_3]$ unit in RSSBO exhibits significant dipole moments (3.82), indicating that RSSBO possesses the capacity to generate a larger second-order microscopic polarizability than KBSBO. In contrast, the non-π-conjugated $[BO_4]$ tetrahedra make less contribution to the overall SHG coefficients due to their smaller dipole moments (Table S6†). Besides, the distortion direction and eccentricity degree (Δd) of the dipole moments were evaluated using the method proposed by Halasyamani (Table S7†), revealing that RSSBO exhibits a larger degree of distortion than its analogous compound KBSBO.[46]

Conclusions

In summary, we successfully synthesized two novel rare-earth borate NLO crystals, KBSBO and RSSBO, by spontaneous crystallization. Structural analyses unveiled an isostructural 3D framework composed of $[ScO_6]$ octahedra and $[B_5O_{10}]$ clusters within these compounds. Leveraging these structural features, KBSBO and RSSBO display remarkably short deep UV absorption cutoff edges below 190 nm, and showcase amplified SHG efficiencies of 1.4 and 2.0 × KDP, respectively. In addition, structural and theoretical analyses indicate that the SHG activity of KBSBO and RSSBO predominantly originates from the $[B_5O_{10}]$ clusters and distorted $[ScO_6]$ octahedra. These findings achieve a good balance between a wide transmission range and a large SHG intensity, thereby expanding the structural chemistry landscape of rare earth borates and inspiring the deliberate fabrication of novel deep UV NLO materials with superior performance.

Data availability

Data available in the ESI† includes the Experimental section and additional tables and figures.

Author contributions

Shuaifeng Li: experiment, investigation, data curation, writing original draft. Weiming Li and Xiang Li: software, formal analysis. Guangsai Yang: formal analysis. Ning Ye, Zhanggui Hu and Yicheng Wu: resources, funding acquisition. Conggang Li: conceptualization, funding acquisition, methodology, project administration, review & editing.

Conflicts of interest

There are no conflicts to declare.

Acknowledgements

This work was supported by the National Key R&D Program of China (2021YFA0717800), National Natural Science Foundation of China (No. 61835014), State Key Laboratory of Crystal Materials, Shandong University (No. KF2303) and Tianjin University of Technology Graduate Research Innovation Practice Project Funding (No. YJ2393).

Notes and references

1 P. Becker, *Adv. Mater.*, 1998, **10**, 979–992.

2 (*a*) P. S. Halasyamani and J. M. Rondinelli, *Nat. Commun.*, 2018, **9**, 2972; (*b*) P. S. Halasyamani and W. Zhang, *Inorg. Chem.*, 2017, **56**, 12077–12085.
3 (*a*) C. Wu, G. Yang, M. Humphrey and C. Zhang, *Coord. Chem. Rev.*, 2018, **375**, 459–488; (*b*) C. Wu, X. Jiang, Y. Hu, C. Jiang, T. Wu, Z. Lin, Z. Huang, M. G. Humphrey and C. Zhang, *Angew. Chem., Int. Ed.*, 2022, **61**, e202115855.
4 (*a*) Q. Liu, Q. Wu, T. Wang, L. Kang, Z. Lin, Y. Wang and M. Xia, *Chin. J. Struct. Chem.*, 2023, **42**, 100026; (*b*) Q. X. Liu, C. Tang, Y. Y. Wen, T. Y. Wang, Q. Wu, C. J. He and M. J. Xia, *Opt. Mater.*, 2023, **137**, 113605.
5 (*a*) M. Mutailipu, K. Poeppelmeier and S. Pan, *Chem. Rev.*, 2021, **121**, 1130–1202; (*b*) Y. Wang and S. Pan, *Coord. Chem. Rev.*, 2016, **323**, 15–35; (*c*) M. Mutailipu, J. Han, Z. Li, F. Li, J. Li, F. Zhang, X. Long, Z. Yang and S. Pan, *Nat. Photonics*, 2023, **17**, 694–701.
6 S. Zhao, L. Kang, Y. Shen, X. Wang, M. A. Asghar, Z. Lin, Y. Xu, S. Zeng, M. Hong and J. Luo, *J. Am. Chem. Soc.*, 2016, **138**, 2961–2964.
7 G. H. Zou and K. M. Ok, *Chem. Sci.*, 2020, **11**, 5404–5409.
8 C. L. Hu and J. G. Mao, *Coord. Chem. Rev.*, 2015, **288**, 1–17.
9 L. Xiong, L. M. Wu and L. Chen, *Angew. Chem., Int. Ed.*, 2021, **60**, 25063–25067.
10 T. T. Tran, N. Z. Koocher, J. M. Rondinelli and P. S. Halasyamani, *Angew. Chem., Int. Ed.*, 2017, **56**, 2969–2973.
11 (*a*) G. Peng, N. Ye, Z. Lin, L. Kang, S. Pan, M. Zhang, C. Lin, X. Long, M. Luo, Y. Chen, Y. Tang, F. Xu and T. Yan, *Angew. Chem., Int. Ed.*, 2018, **57**, 8968–8972; (*b*) M. Luo, F. Liang, Y. X. Song, D. Zhao, F. Xu, N. Ye and Z. S. Lin, *J. Am. Chem. Soc.*, 2018, **140**, 3884–3887.
12 Y. Q. Li, W. Q. Huang, Y. Zhou, X. Y. Song, J. Zheng, Y. H. Wang, Y. P. Song, M. J. Li, J. H. Luo and S. G. Zhao, *Angew. Chem., Int. Ed.*, 2023, **62**, e202215145.
13 M. Mutailipu, Z. Yang and S. Pan, *Acc. Mater. Res.*, 2021, **2**, 282–291.
14 (*a*) X. Liu, L. Kang, P. Gong and Z. Lin, *Angew. Chem., Int. Ed.*, 2021, **60**, 13574–13578; (*b*) S. P. Guo, X. Y. Cheng, Z. D. Sun, Y. Chi, B. W. Liu, X. M. Jiang, S. F. Li, H. G. Xue, S. Q. Deng, V. Duppel, J. Köhler and G. C. Guo, *Angew. Chem., Int. Ed.*, 2019, **58**, 8087–8091.
15 J. Song, C. G. Li, J. M. Jiao, Y. H. She, W. L. Zhao, F. Liang, N. Ye, Z. G. Hu and Y. C. Wu, *Inorg. Chem. Front.*, 2023, **10**, 5488–5495.
16 X. Liu, Y. C. Yang, M. Y. Li, L. Chen and M. Wu, *Chem. Soc. Rev.*, 2023, **52**, 8699–8720.
17 R. L. Tang, W. Xu, W. J. Xie and C. L. Hu, *Inorg. Chem. Front.*, 2022, **9**, 5153–5160.
18 N. Ye, W. Zeng, B. Wu and C. Chen, *Proc. SPIE*, 1998, **3556**, 21–23.
19 W. Zhang, X. Hou, S. Han and S. Pan, *Coord. Chem. Rev.*, 2024, **505**, 215664.
20 M. J. Xia, X. X. Jiang, Z. S. Lin and R. K. Li, *J. Am. Chem. Soc.*, 2016, **138**, 14190–14193.
21 M. Mutailipu, F. Li, C. Jin, Z. Yang, K. R. Poeppelmeier and S. Pan, *Angew. Chem., Int. Ed.*, 2022, **61**, e202202096.
22 S. S. Li, X. M. Liu, H. P. Wu, Z. F. Song, H. W. Yu, Z. S. Lin, Z. G. Hu, J. Y. Wang and Y. C. Wu, *Chem. Sci.*, 2021, **12**, 13897–13901.
23 H. W. Yu, H. P. Wu, S. L. Pan, Z. H. Yang, X. L. Hou, X. Su, Q. Jing, K. R. Poeppelmeier and J. M. Rondinelli, *J. Am. Chem. Soc.*, 2014, **136**, 1264–1267.
24 H. Qiu, F. Li, Z. Li, Z. Yang, S. Pan and M. Mutailipu, *J. Am. Chem. Soc.*, 2023, **145**, 24401–24407.
25 R. Komatsu, T. Sugawara, K. Sassa, N. Sarukura, Z. Liu, S. Izumida, Y. Segawa, S. Uda, T. Fukuda and K. Yamanouchi, *Appl. Phys. Lett.*, 1997, **70**, 3492–3494.
26 N. Umemura and K. Kato, *Appl. Opt.*, 1996, **35**, 5332–5335.
27 I. Makoto, K. Taisuke, F. Hiroyuki, M. Yusuke and S. Takatomo, *J. Appl. Phys.*, 1997, **36**, L276–L279.
28 Y. Cheng, F. Liang, D. Lu, D. Lu, J. Feng, G. Zhang, H. Yu, H. Zhang and Y. Wu, *Light: Sci. Appl.*, 2023, **12**, 203.
29 M. Mutailipu, Z. Xie, X. Su, M. Zhang, Y. Wang, Z. Yang, M. Janjua and S. Pan, *J. Am. Chem. Soc.*, 2017, **139**, 18397–18405.
30 H. P. Wu, H. W. Yu, S. L. Pan, Z. J. Huang, Z. H. Yang, X. Su and K. R. Poeppelmeier, *Angew. Chem., Int. Ed.*, 2013, **52**, 3406–3410.
31 S. Neumair, J. Knyrim, O. Oeckler, R. Glaum, R. Kaindl, R. Stalder and H. Huppertz, *Chem.–Eur. J.*, 2010, **16**, 13659.
32 Z. Xie, M. Mutailipu, G. He, G. Han, Y. Wang, Z. Yang, M. Zhang and S. Pan, *Chem. Mater.*, 2018, **30**, 2414–2423.
33 M. Mutailipu, Z. Xie, X. Su, M. Zhang, Y. Wang, Z. Yang, M. Janjua and S. Pan, *J. Am. Chem. Soc.*, 2017, **139**, 18397–18405.
34 W. Liu, X. M. Liu, J. Shen, Y. F. Li, H. M. Song, J. C. Feng, Z. S. Lin and G. C. Zhang, *Dalton Trans.*, 2020, **49**, 9355–9361.
35 S. Zhao, G. Zhang, J. Yao and Y. Wu, *Mater. Res. Bull.*, 2012, **47**, 3810–3813.
36 Z. Jia, Q. Zeng, P. Gong, Y. Dong, X. Zhang, B. Xin, Z. Lin and M. Xia, *Inorg. Chem.*, 2020, **59**, 13029–13033.
37 V. Atuchin, A. Subanakov, A. Aleksandrovsky, B. Bazarov, J. Bazarova, S. Dorzhieva, T. Gavrilova, A. Krylov, M. Molokeev, A. Oreshonkov, A. Pugachev, Y. Tushinova and A. Yelisseyev, *Adv. Powder Technol.*, 2017, **28**, 1309–1315.
38 J. H. Feng, X. Xu, C. L. Hu and J. G. Mao, *Inorg. Chem.*, 2019, **58**, 2833–2839.
39 S. Zhao, G. Zhang, J. Yao and Y. Wu, *CrystEngComm*, 2012, **14**, 5209–5214.
40 C. Wu, Y. Dang, J. Chen, X. Hou and H. Shi, *Cryst. Growth Des.*, 2023, **23**, 6885–6893.
41 Y. F. Li, F. Liang, H. M. Song, W. Liu, Z. S. Lin and G. C., *Inorg. Chem.*, 2019, **58**, 8943–8947.
42 W. H. Liu, M. H. Lee, R. X. Guo and J. Y. Yao, *Dalton Trans.*, 2023, **52**, 3344–3350.
43 J. Tauc, *Mater. Res. Bull.*, 1970, **5**, 721–730.
44 J. Klein, L. Kampermann, B. Mockenhaupt, M. Behrens, J. Strunk and G. Bacher, *Adv. Funct. Mater.*, 2023, **33**, 2304523.
45 S. K. Kurtz and T. T. Perry, *J. Appl. Phys.*, 1968, **39**, 3798–3813.
46 P. S. Halasyamani, *Metals Chem. Mater.*, 2004, **16**, 3586–3592.